11

Titanium Dioxide Nanomaterials: Basics and Design, Synthesis and Applications in Solar Energy Utilization Techniques

Fuqiang Huang, Yaoming Wang, Jianjun Wu and Xujie Lü
Shanghai Institute of Ceramics, Chinese Academy of Sciences
People's Republic of China

1. Introduction

Titanium dioxide (TiO_2) nanomaterials have been extensively studied in the last two decades. Due to their versatile properties, TiO_2 nanomaterials have possessed themselves vast applications, including paint, toothpaste, UV protection, photocatalysis, photovoltaics, sensing, electrochromics, as well as photochromics. An in-depth study of the basic material properties, electrical transport-favored nano/micro-structure design and processing of TiO_2 nanomaterials will be present in this chapter, focusing on solar energy utilization efficiency enhancement.

2. Basics and design

2.1 A criterion for ranking the charge separation abilities of semiconductors

Nanomaterials used for gathering solar energy inevitably involve charge transport process, and solar energy utilization efficiency often comes down due to the difficulty of charge separation in many material systems, TiO_2 nanomaterials are not exceptional. How to evaluate the charge separation/transport abilities of TiO_2 and other semiconductors is an urgent question to be answered. Solving this problem will give an insight into intrinsic nature of compounds and bring great convenience to material & device design.

Here we have developed the packing factor (PF) concept to evaluate inherently existing internal fields that can be used to rank the charge separation abilities among oxide materials (Lin et al., 2009). The concept is based on the idea that lower elastic stiffness can promote distortion, which promotes internal field, and it can be easily implemented using the packing factor. This packing factor model is a broadly applicable criterion for ranking charge seperation/transport and photocatalytic ability of the materials with similar chemistry or structure. Lower PF value results in lower elastic stiffness, higher internal field, more efficient light-induced electron-hole separation and transport, and higher photocatalytic activity.

PF of a compound was computed by dividing the sum of spherical volumes by the unit cell volume, as seen in the equation of $PF = Z\,(xV_A+yV_B+zV_C)/V_{cell}$, where Z is the number of the formula unit in one unit cell of a semiconductor ($A_xB_yC_z$); V_A, V_B and V_C are ion volumes calculated by assuming spherical ions with a Shannon radius that depends on the

coordination number; and V_{cell} is the cell volume. The different compounds are attributed to the atoms to be packed in their preferred ways to gain the lowest total energy in light of physics. Therefore, the crystal packing factor is not only related to mass density, packing manners, bonding habits, etc. in the crystal structure, but also related to charge density, band width, band gap, carrier mobility, etc. in the electronic structure.

As the two most investigated phases of TiO_2, anatase is widely reported more photocatalytically active than rutile (Yu & Wang, 2007). Meanwhile in our experiments, the different representative organic pollutants (methyl orange, methyl blue, and phenol) for photocatalysis were used to test the activity, but the measured activity trend remains the same, anatase (PF= 0.6455) > rutile (PF= 0.7045). Besides organic pollutant photodegradation, photoinduced water splitting over TiO_2 is also adopted as primary evaluation means to scale the photocatalytic activity. The same activity sequence is obtained, the same as that for dye degradation and mineralization described above. As known, anatase TiO_2 (density = 3.90 g/cm^3, PF = 0.6455) is a more loosely packed structure compared to rutile (density = 4.27 g/cm^3, PF = 0.7045). The loosely packed structure of anatase TiO_2 is favorable for photocatalytic activity.

Based on the lifetime and mobility of electrons and holes, we can give a full explanation from the packing factor model. It is conceivable that photocatalytically active ion in a lower PF structure is more polarizable, therefore its exciton radius is larger as are the lifetimes of electrons and holes. In addition, a lower PF structure is more deformable, which lowers the activation (hopping) barrier for polarons (e.g., those associated with O^-) thus increasing their mobility. The band dispersion often associated with low PF structures may additionally increase the dispersion at the edges of CBM and VBM, thus decreasing the effective mass of electrons and holes. This would further contribute to a higher mobility. These generic mechanisms may operate in a broad range of structures and at selected sites where photoelectrons and holes are generated and transported. Consequently, they could lead to wide applicability of the PF model.

The packing factor model — lower PF value results in more efficient light-induced electron-hole separation and transport, can also explains that anatase TiO_2 with a better charge transport ability than rutile TiO_2 has been broadly used as the sensitized electrode of dye-sensitized solar cells (DSC). Meanwhile, the PF model also gained wide supports from the literatures covering compounds of d^0 cations (Ti^{4+}, V^{5+}, Nb^{5+}, Ta^{5+}, Cr^{6+}, Mo^{6+} and W^{6+}) and d^{10} cations (Ag^+, Zn^{2+}, Cd^{2+}, Ga^{3+}, In^{3+}, Sn^{4+} and Sb^{5+}). So far, the PF model has been proven by over 60 systems covering about 120 photocatalysts (Lin et al., 2009). The finding not only provides a new focus on ranking the charge separation and transport abilities for DSC electrode materials, but also discloses insights for developing new photocatalysts with high UV- and/or visible-light responsive activities.

2.2 Electrical transport and charge separation favored nano/micro-structure design

Charge transport is of great importance for the performance of electronic devices, especially for those solar energy gathering devices, such as solar cells, photocatalysts, and chlorophylls in photosynthesis, etc. On one hand, the transport behavior of sensitized anode electrode TiO_2 for DSCs or new concept solar cells is attributed to the carrier (electron) concentration and mobility. The high electron mobility in TiO_2 relies on the high crystallinity of the lattice, while the crystallinity is closely related to the preparation condictions. We have successfully controlled the crystallinity of TiO_2 via varying the reaction temperature and solvents. The

effect of the crystallinity on charge transport and separation has been also fully discussed. On the other hand, the charge transport properties of single and/or conventional materials may not be sufficient. Nano/micro-structure materials design offers a powerful approach for tailoring the transport property and charge separation ability, and great enhancement in performance can be expected. We successfully designed two kinds of nano/micro-structure configurations as sensitized anode for DSCs, one is *electron-transport favored semiconductor*, and the other is *composite structure of TiO_2 | semimetal | semiconductor*.

The sensitized anode for DSCs is preferred to be an excellent electron conductor, and its conduction band should match the dye's LUMO (the lowest unoccupied molecular orbitals). Furthermore, a tightly chemical binding interface is necessary for electron-transfer from dye to TiO_2 and between the TiO_2 particles. Nb-doped TiO_2 has also appeared to have promising applications on transparent conducting oxide (TCO) (Furubayashi et al., 2005), antistatic material, and gas sensor (Sharma et al., 1998). However, few studies have been reported on the positive roles of Nb-doped TiO_2 nanoparticles applied as the photoanode material of DSCs, and the mechanism of the effects by ion doping is still controversial. In this chapter, the Nb-doped TiO_2 nanocrystalline powders were demonstrated to be an *electron-injection and transport favored semiconductor* to enhance the performance of dye-sensitized solar cells. The improvement was ascribed to the enhanced electron injection and transfer efficiency caused by positive shift of flat-band potential (V_{fb}) and increased powder conductivity (Lü etal., 2010).

A new composite structure of *TiO_2 | semimetal | semiconductor* have been investigated to promote charge separation and electron transport. In general, such heterojunction structure requires (1) an alignment of the conduction band of the *semiconductor* with that of TiO_2, (2) little solubility of the *semiconductor* in TiO_2, (3) a highly conductive *semimetal* interface such as transparent conducting oxide (TCO), and (4) a high electron mobility in the *semiconductor*. One example is TiO_2|ZnO:Ti|ZnO, in which ZnO has a similar band structure but much higher electron mobility (205–300 $cm^2\ V\ s^{-1}$) than TiO_2 (0.1–4 $cm^2\ V\ s^{-1}$) (Zhang et al., 2009), Zn^{2+} has very low solubility in TiO_2 (Bouchet et al., 2003), and the Ti-doped ZnO (ZnO:Ti) is a TCO with a high conductivity (up to 1.5×10^3 S cm^{-1}) that depends on the doping level and microstructure (Chung etal., 2008). In this chapter, the new composite construct with a hollow spherical geometry with a hybrid TiO_2/ZnO composition is proposed for solar energy utilization. The hybrid TiO_2/ZnO spheres exhibit enhanced energy-conversion efficiency for the DSC. These improvements are ascribed to the enhanced charge-separation and electron-transport efficiencies made possible by the nano-heterojunction structure of TiO_2|ZnO:Ti|ZnO.

3. Synthesis and applications

3.1 Crystallinity control and solvent effect

As a bottom-up method, solvothermal method is a facile route for direct synthesis of nano-TiO_2. However, the main attention is often directed toward control over the structure and morphology only by varying the reaction temperature, duration, additive, and pH value during solvothermal treatment, while the solvent has rarely been deliberately selected to achieve different well-crystallized nanostructures. Initial failures in the solvothermal growth of a specific compound are usually the result of lack of proper data on the type of solvents, the solubility, and solvent-solute interaction. Solubility is a vital physicochemical and technological parameter which strongly influences the rate of dissolution, the degree of the supersaturation, thus the rate of nuclei formation. Solubility depends upon the nature of the

substance, its aggregate state, temperature, pressure and a series of other factors, among which, the dielectric constant has a crucial effect on the solubility of precursor due to the diverse solvation energy. We have studied the formation of well-crystallized nano-TiO_2 on the basis of a one-pot solvothermal route. The effect of the dielectric constant on the solubility of the precursor, the nucleation and the crystal growth was discussed in detail. Moreover, the photocatalytic activity of the samples was also fully investigated in close conjunction with crystallinity (Wu et al., 2009).

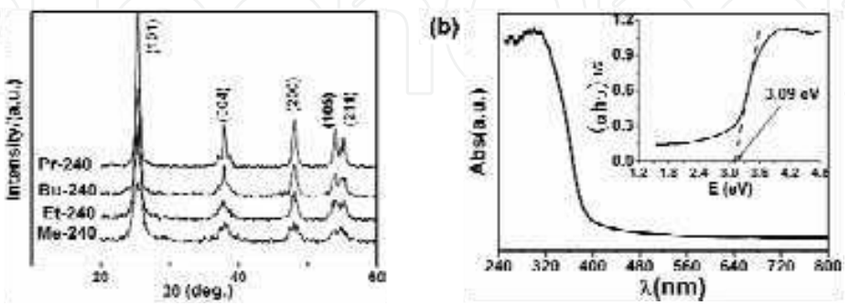

Fig. 1. (a) XRD patterns for samples at 240 °C. Et here shows the first two letters of the solvent (ethanol). Me, Pr and Bu are for methanol, 2-propanol and n-butanol, respectively. (b) UV-Vis spectrum for a typical nano-TiO_2

Fig. 1a presents the XRD patterns for the powders synthesized in the four different alcohols. Hereafter, Et-240 was denoted for nano-TiO_2 treated at 240 °C for 6 h with ethanol as solvent. All of the powders belong to the anatase type of TiO_2 (JCPDS No. 21-1272). Moreover, Pr-240 obtained the sharpest peaks when the temperature was set at 240 °C, indicating the relatively high crystallinity was obtained by these two samples. A typical UV-Vis spectrum for the obtained nano-TiO_2 was shown in the Fig. 1b. To obtain more precise optical band gap, plots of $(\alpha h\nu)^{1/2}$ vs the energy of absorbed is used to obtain the band gap because of its indirect transition nature (Tian et al., 2008). Eg was determined to be 3.09 eV.

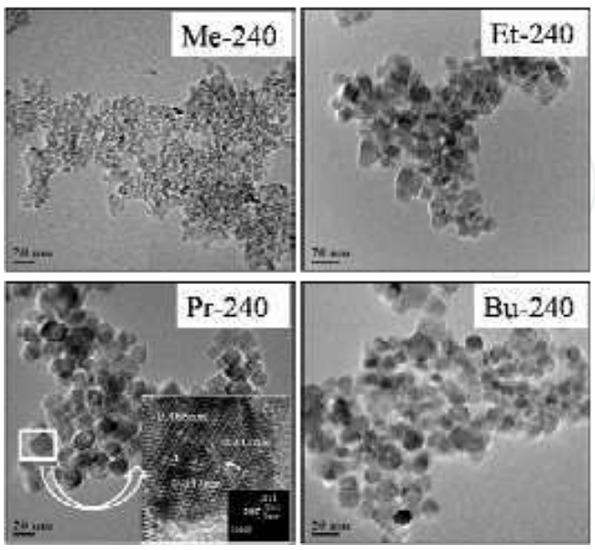

Fig. 2. TEM images for the TiO_2 nanoparticles at 240 °C

The TEM images for samples obtained at 240 °C were presented in Fig. 2. The crystallite size and shape strongly depend on the type of the solvent employed. Particles with amorphous shape are severely agglomerated and poor-crystallized in the case of methanol. While for Pr-240, the crystallinity is greatly enhanced and the shape tends to exhibit equiaxed geometry bounded by crystallographic facets. Additionally, HRTEM observation confirms the anatase structure for Pr-240. The inset shows the lattice image of a TiO_2 grain and its FFT diffractogram which is consistent to a [100]-projected diffraction pattern of the anatase TiO_2. Among the all four powders obtained at 240 °C, Pr-240 has obtained the largest crystallite size of about 15 nm determined from the corresponding TEM image. Considering that the samples prepared in the present work are synthesized under the same conditions, *i.e.*, temperature and time, the varied morphology and XRD patterns of the powders should originate from the different solvents for their distinct physicochemical properties.

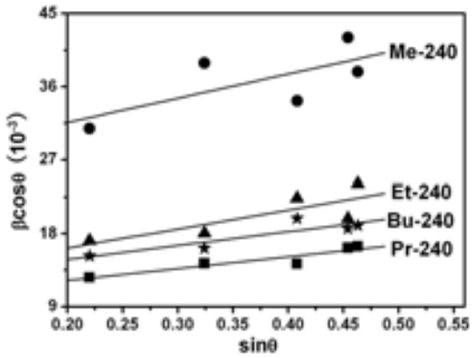

Fig. 3. The relation between βcosθ and sinθ for the samples

Crystallite size (D) and lattice strain (ε) are calculated via the Williams and Hall equation, $\beta\cos\theta = K\lambda / D + 2\varepsilon \sin\theta$, plots of βcosθ against sinθ based on the XRD patterns (Fig. 1a) are shown in Fig. 3. For Et-240, Bu-240 and Pr-240, it shows relatively good linearity, which gives reliable values of D and ε. Table 1 depicts the quantitative values of D and ε for each sample. Crystallinity enhances, *i.e.*, the growth of crystallite and the decrease in lattice strain, in the order: Me-240, Et-240, Bu-240 and Pr-240, indicating that the crystallinity for the nano-TiO_2 has a strong dependence on the solvent used

Catalyst	D (nm)	ε (10^{-3})
Me-240	5.7	14.94
Et-240	11.6	11.87
Bu-240	12.2	8.56
Pr-240	14.8	7.27

Table 1. The obtained D and ε based on the data shown in Fig. 3

Solvents with different physicochemical properties have a pronounced effect on the crystallinity and morphology of the final nanocrystals by influencing the solubility, reactivity, diffusion behavior and the crystallization kinetics (crystal nucleation and growth rate). Here, we give a closer look on the effect of dielectric constant on the crystallinity of the

obtained nano-TiO_2. The crystallization for nanoparticles generally consists of two processes (Sirachaya et al., 2006): nucleation and crystal growth. The nucleation rate, J_N, can be expressed as follows with a pre-factor, J_0:

$$J_N = J_0 \exp\left(\frac{-16\pi V_m^2 \gamma^3}{3(RT)^3 (\ln S)^2}\right)$$

Where V_m is the molar volume of the solid material, S is the supersaturation degree, and $S = C_l / C_s$. C_l the precursor concentration, C_s the solubility of the solid phase, J_0 the frequency of collisions between precursor molecules, γ the interfacial tension, R the gas constant, and T the temperature. Hence, it can be concluded that the nucleation rate is expected to increase strongly with increasing supersaturation. The solubility of an inorganic salt decreases with a decrease in the dielectric constant of the solvent, due to the decreased solvation energy. Meanwhile, during the process of the crystal growth, larger particles grow at the expense of the smaller ones owing to the energy difference between the larger particles and the smaller ones of a higher solubility based on the Gibbs-Thompson law. This refers to the "Ostwald ripening" process applied and confirmed in numbers of papers (Li et al., 2007). In methanol, as Table 2 shows, a higher dielectric constant (η = 32.35) invites a higher solubility of the solid metal oxide and a lower supersaturation degree in this system, which predicts less nuclei numbers, inadequate nutriments-supply and slower crystal-growth rates (Hua et al., 2006), thus lower crystallinity. As mentioned above, the crystallinity (concerning two part: crystallite size and lattice strain) of the obtained nano-TiO_2 should be foretold in the enhanced order: Me-240 **<** Et-240 **<** Pr-240 **<** Bu-240. However, the present data show some unexpected results, *i.e.*, Pr-240 obtains a better crystallization than Bu-240, demonstrating that other properties of the solvent, such as viscosity, saturated vapor pressure, coordinating ability and steric hindrance should be taken into account (Zhang et al., 2002). In other words, crystallinity depends on dielectric constant of the solvent to a great extent, not in all the range.

Solvent	Methanol	Ethanol	2-Propanol	n-butanol
η	32.35	25.00	18.62	17.50

Table 2. Dielectric constant for the alcohols used, η refers to dielectric constant, and the values are provided by (Moon et al., 1995).

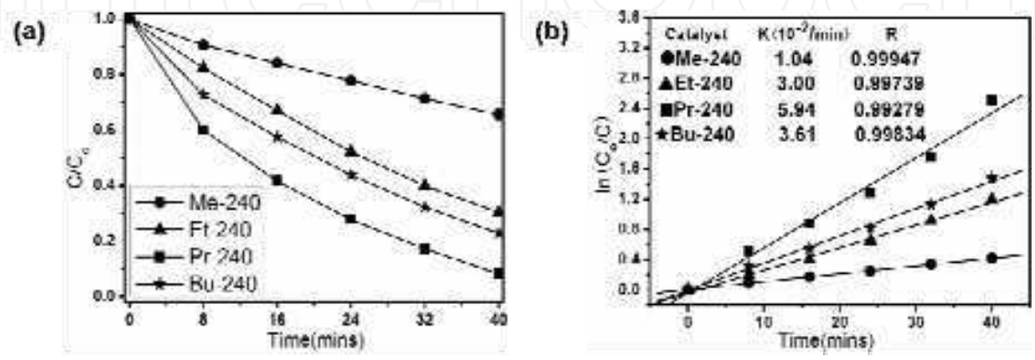

Fig. 4. MO photodegradation over samples under UV-light irradiation

Fig. 4 depicts the result of the photocatalytic degradation of methyl orange (MO) for nano-TiO_2. The photocatalysis efficiency decreases gradually in the order: Pr-240 > Bu-240 > Et-240 > Me-240, in an agreement with the tendency of the crystallite size, as shown in Table 1. In other words, the photocatalytic efficiency increased in the order: Me-240 **<** Et-240 **<** Bu-240 **<** Pr-240, simultaneously with an increase of the crystallinity, *i.e.*, the increase in crystallite size and the decrease in lattice strain, as Fig. 5 shows, confirming the dependence of the photocatalysis on the crystallinity.

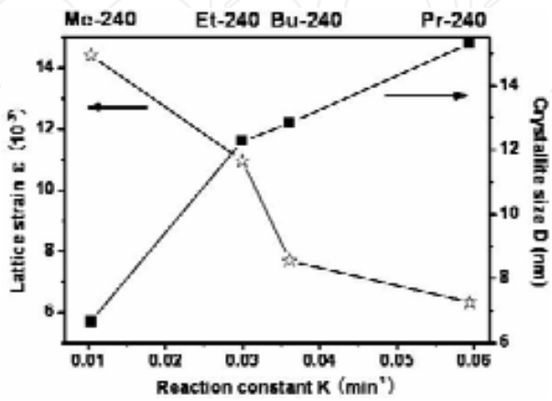

Fig. 5. The effect of the crystallinity on the reaction constant K

Crystallinity was proved to have an indispensible effect on the two most important processes of the photocatalysis: charges separation and charges transport, as follows (Chen & Mao, 2007): (1) the highly crystallized anatase can promote the charges transfer from particle center to surface. The residual strain of the poor-crystallized TiO_2 lattice leads to disorder and distortion of the TiO_2 matrix, which have a severe scattering effect on the charges transport. Furthermore, an electron and a hole can migrate a longer distance in a crystal of larger crystallite size than in a smaller one, separating more the reducing and oxidizing sites on the surface of the crystal. So the volume recombination may occur less frequently; (2) it eliminates the crystal defects, *i.e.*, impurities, dangling bonds, and microvoids, which behave as recombination centers for the e^-/h^+ pairs, thus the surface recombination is greatly suppressed. It is, thus, no wonder that Pr-240 of which the crystallite size is about 14.8 nm and lattice strain about 7.27×10^{-3} holds the maximum in the reaction constant K of MO decomposition, *i.e.*, about 6 times of that for Me-240.

3.2 Synthesis and solar-spectrum tunable TiO_2: Eu

Extensive research interests are focused in photocatalysis, but investigations and applications for the photoluminescence (PL) properties of TiO_2 have not been simultaneously satisfied. As we konw, high-energy photons (UV, etc.) in the solar spectrum are harmful to the components of DSCs (dye dissociation) and silicon solar cells (overheated silicon). Based on our recent study of TiO_2: Eu (Wu etal., 2010), through the excition at 394 nm (UV) and 464 nm (blue light), it shows intense emissions at 592 nm (yellow) and 612 nm (red). In other words, TiO_2: Eu can be used as a solar-spectrum tunable photoluminescent material to convert high-energy photons to low-energy photons, *i.e.,* from UV and/or blue to yellow or red light. The PL process of TiO_2: Eu comprises the intrinsic excitation resulted from the *f-f* inner-shell transitions and the host excitation ascribed to the charge transfer

band (CTB) from O–Ti to Eu^{3+} ions. It requires a perfect lattice of TiO_2 for charges transfer, in order to avoid space charge regions and e-h recombination. So the crystallinity of the TiO_2 lattice is to have a pronounced effect on the PL process, which should be further investigated.

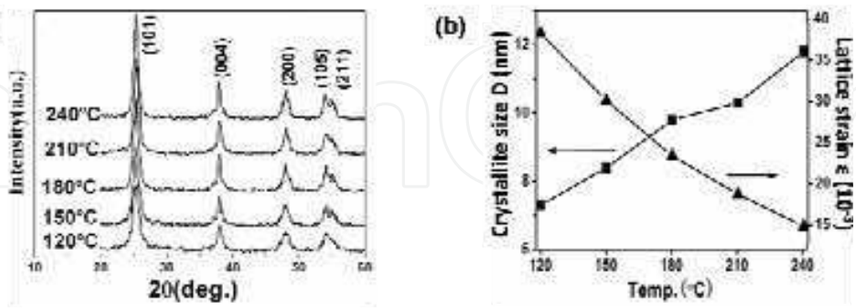

Fig. 6. (a) XRD patterns and (b) the corresponding crystallite size D and lattice strain ε for the TiO_2: Eu nanoparticles on the hydrothermal temperature

Based on the Williams and Hall Equation, D increases from 7.3 nm to 11.8 nm and ε decreases from 38.25 × 10^{-3} to 14.82 × 10^{-3} for the TiO_2: Eu samples when increasing the hydrothermal temperature (Fig. 6). The growth of crystallite and the decrease in lattice strain, indicating that the crystallinity of the nanoparticles has been enhanced, and that various structural defects, such as small displacement of atoms neighboring, non-uniform strain and residual stress of the lattice, have been gradually eliminated. These defects were reasonably supposed to influence the PL performance.

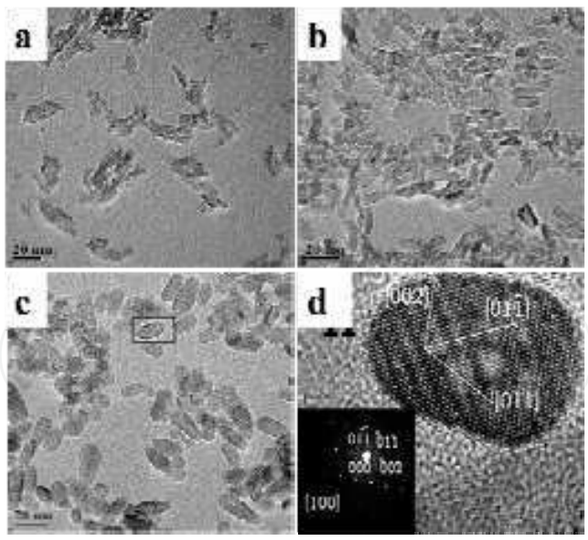

Fig. 7. The TEM images of (a) Eu^{3+}/TiO_2-120, (b) Eu^{3+}/TiO_2-180, (c) Eu^{3+}/TiO_2-240, (d) HRTEM of Eu^{3+}/TiO_2-240, Fast-Fourier Transformed diffractogram of Eu^{3+}/TiO_2-240 (inset)

The morphology of the nanoparticles changes from polyhedron to rod-like with Eu^{3+} doping (Fig. 7), which implies that the Eu^{3+} doping plays an important effect on the crystallographic orientation of TiO_2 nanocrystal. Eu^{3+} hinders the growth of specific facets of anatase TiO_2 based on the "oriented attachment" mechanism (Ghosh & Patra, 2007). The similar case was

also observed in Er^{3+}-doped TiO_2. And HRTEM of a representative rod also shows its anatase structure, and the corresponding FFT diffractogram demonstrate its single crystal nature (Fig. 7d).

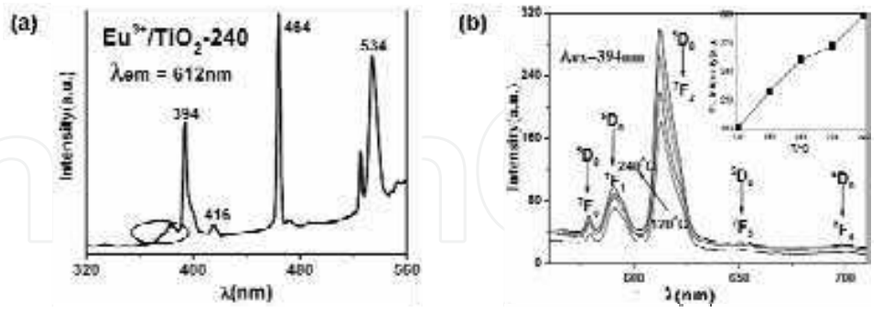

Fig. 8. (a) The excitation spectrum of Eu^{3+}/TiO_2-240 (λ_{em} = 612 nm), (b) the emission spectra (λ_{ex} = 394 nm) of the TiO_2:Eu^{3+} samples, where their maximum emission (λ_{em} = 612 nm) intensities at 612 nm in the inset

Fig. 8a depicts the typical excitation spectrum of the Eu^{3+}/TiO_2-240. By monitoring the emission line of 612 nm, the excitation lines appear at 394, 416, 464, and 534 nm are ascribed to the *f-f* inner-shell transitions within the Eu^{3+} $4f^6$ configuration. Besides, a new band appears in the range from 320 to 380 nm, although it's not obvious. Based on the previous papers, the new wide band can be attributed to the host excitation and assigned to the charge transfer band (CTB) from O–Ti to the Eu^{3+} ions. Similar broad band has also been observed and attributed to the CTB from O–Ti to Eu^{3+} ions in the previous works (You & Nogami, 2004).

Sample	I [$^5D_0 \rightarrow {}^7F_2$] (a.u.)	I [$^5D_0 \rightarrow {}^7F_1$] (a.u.)	R
Eu^{3+}/TiO_2-120	2.324	0.901	2.58
Eu^{3+}/TiO_2-150	2.793	1.054	2.65
Eu^{3+}/TiO_2-180	3.228	1.117	2.89
Eu^{3+}/TiO_2-210	3.415	1.149	2.97
Eu^{3+}/TiO_2-240	3.822	1.258	3.05

Table 3. The integrated intensity ratio of $^5D_0 \rightarrow {}^7F_2$ / $^5D_0 \rightarrow {}^7F_1$ of the samples. **R:** Integrated intensity ratio of $^5D_0 \rightarrow {}^7F_2$ and $^5D_0 \rightarrow {}^7F_1$

The five characteristic peaks at 579, 592, 612, 651, 699 nm corresponding to $^5D_0 \rightarrow {}^7F_0$, $^5D_0 \rightarrow {}^7F_1$, $^5D_0 \rightarrow {}^7F_2$, $^5D_0 \rightarrow {}^7F_3$, $^5D_0 \rightarrow {}^7F_4$ transitions of Eu^{3+} ion, respectively, are observed for all the Eu^{3+} doped samples at the excitation wavelength of 394 nm in Fig. 8b. It can be seen that the $^5D_0$ emission is intensified with the increment in temperature accompanied with gradually enhanced crystallnity. For $^5D_0 \rightarrow {}^7F_2$ transition, the PL intensity was quantitatively analysed and tabulated in the inset of Fig. 8b. The intensity ratio (R) of $^5D_0 \rightarrow {}^7F_2$ (612 nm) to

$^5D_0 \rightarrow {}^7F_1$ (592 nm) increases as the degree of Eu–O covalence increases, so R is widely used to investigate the bonding environment of the Eu^{3+} ions. The integrated intensity ratio (R) of the samples obtained at different temperature are shown in Table 3.Note that R increases with hydrothermal temperature, accompanied with the promoted crystallinity, indicating that the covalence degree of the Eu^{3+} ions increases.

On the other hand, the great mismatch of ionic radius between Eu^{3+} (0.95 Å) and Ti^{4+} (0.68 Å) makes the doping Eu^{3+} hardly enter into the TiO_2 lattice (Lin & Yu, 1998), but inclined to distribute in the crystallite surface or interstitials of TiO_2 nanocrystals. For the poor-crystallized TiO_2 matrix, the Eu^{3+} has a tendency to form clusters due to the reduction of Eu^{3+}–Eu^{3+}distances (Stone et al., 1997). The clusters are undesirable which lead to an enhanced interparticle contact of the Eu–Eu pairs, thus quench its luminescence through cross relaxation. As the crystallinity enhances, the gradual formation of Eu^{3+}–O^{2-}–Ti^{4+} bonding leads to reducing the extent of the Eu^{3+} clusters, suppressing the cross relaxation and intensifying the luminescence effectively. Furthermore, the great elimination of the crystal defects, as quenching centers for luminescence, can diminish the undesired nonradiative recombination routes for electrons and holes (Ikeda et al., 2008), contributing to the enhanced luminescence.

3.3 Synthesis and application of TiO_2: Nb in DSCs

The highly crystallized Nb-doped TiO_2 nanoparticles were prepared by a one-step hydrothermal process and applied as the photoanode materials in DSCs, which facilitate electron injection and transfer, contributing to the significant improvement of energy conversion efficiency of the DSCs. The mechanism of the improvement caused by Nb doping was discussed in detail.

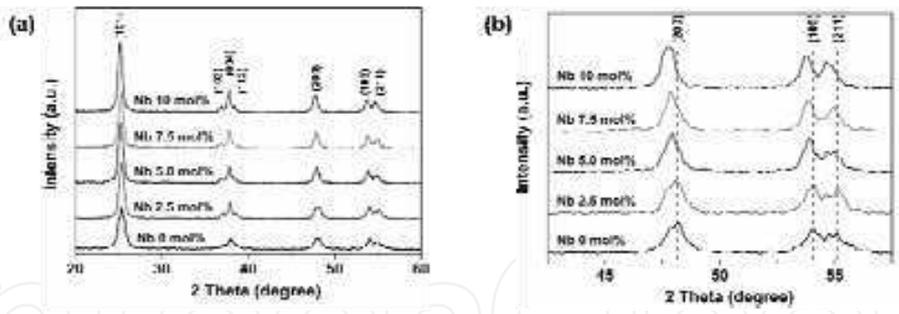

Fig. 9. (a) XRD patterns of as-prepared samples with different Nb contents; (b) Details of the XRD patterns around 48° and 54° 2θ values

Fig. 9 shows the XRD patterns of the Nb-doped TiO_2 with different Nb contents. All peaks of the as-prepared samples can be assigned to the anatase phase, indicating that the anatase nanocrystalline structure is retained after doping. The diffraction peaks shift to lower theta values with increasing Nb content, due to the larger radius of Nb^{5+} (0.64 Å) than Ti^{4+} (0.61 Å) according to the Bragg equation of $2d\sin\theta = \lambda$ (Fig. 9b). Furthermore, the intensity of the diffraction peaks strengthens gradually with the increasing Nb content. Consequently, as the superiority of the new method, the higher ordered nature of the TiO_2 nanoparticles introduced by the Nb doping would be in favor of electron transfer, resulting in the increased photocurrent. The HRTEM images in Fig. 10 indicate the high crystallinity of the TiO_2 nanoparticles.

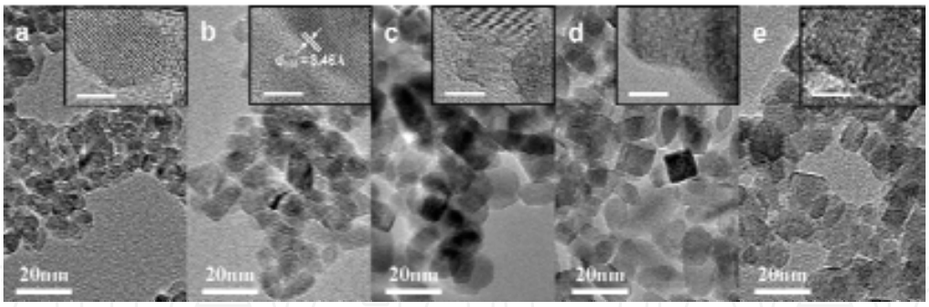

Fig. 10. TEM images of the as-prepared TiO_2 nanoparticles with different Nb contents (a) 0 mol%, (b) 2.5 mol%, (c) 5.0 mol%, (d) 7.5 mol%, and (e) 10.0 mol%. Inset shows the corresponding HRTEM image of each sample (Scale bar 5 nm)

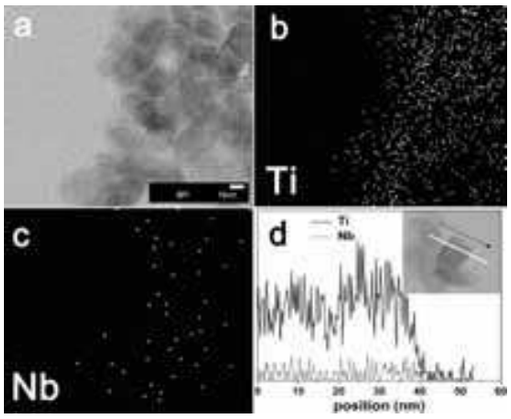

Fig. 11. (a) Bright-field STEM image of 5.0 mol% Nb-doped TiO_2; (b, c) the corresponding elemental mapping of Ti (b) and Nb (c); (d) line-scanning analysis across the nanoparticles indicated by the line as shown in the inset

Fig. 11 shows the STEM image of 5.0 mol% Nb-doped TiO_2 nanoparticles, and the corresponding elemental mapping, revealing the homogeneous spatial distribution of Nb. The uniform distribution of Nb in the TiO_2 lattice was also confirmed by the line-scanning analysis (Fig. 11d).

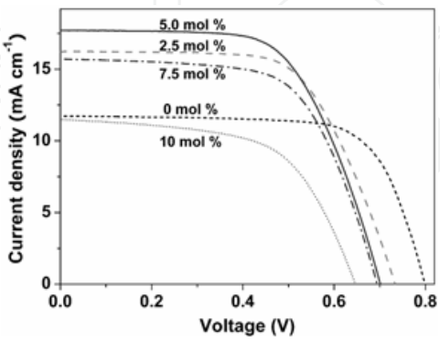

Fig. 12. Current – voltage curves of dye-sensitized solar cells based on the undoped and Nb-doped TiO_2 electrodes

Fig. 12 shows the current-voltage curves of the open cells based on the Nb-doped and undoped TiO_2 photoelectrodes. The performance characteristics are summarized in Table 4.

A pronounced increase in the photocurrent for the DSCs based on the Nb-doped TiO_2 was observed by the Nb doping between 2.5 – 7.5 mol%. As a result, an improved energy conversion efficiency of 7.8% was achieved for DSC based on the 5.0 mol% Nb-doped TiO_2, which was 18.2% higher than that of the undoped one. Whereas, the influence on the open circuit potential (V_{oc}) by the doping of Nb is negative. It is evident that the conduction band edge has been changed by the Nb doping.

DSCs	J_{sc} [mA cm^{-2}]	V_{oc} [V]	FF [%]	η [%]	amount of dye [a] [mol cm^{-2}] × 10^{-8}	film thickness [b] [μm]
0 mol%	11.87 ± 0.26	0.79 ± 0.01	70 ± 1	6.6 ± 0.1	5.2 ± 0.7	5.5 ± 0.2
2.5 mol%	15.75 ± 0.51	0.74 ± 0.01	64 ± 1	7.5 ± 0.3	5.5 ± 0.6	5.4 ± 0.3
5.0 mol%	17.67 ± 0.19	0.70 ± 0.01	63 ± 1	7.8 ± 0.2	5.4 ± 0.3	5.4 ± 0.2
7.5 mol%	15.91 ± 0.22	0.69 ± 0.01	63 ± 2	6.9 ± 0.2	5.7 ± 0.2	5.5 ± 0.2
10.0 mol%	11.79 ± 0.57	0.65 ± 0.01	57 ± 3	4.4 ± 0.2	5.1 ± 0.9	5.4 ± 0.5

Table 4. Performance characteristics of dye-sensitized solar cells based on the undoped and Nb-doped TiO_2 electrodes

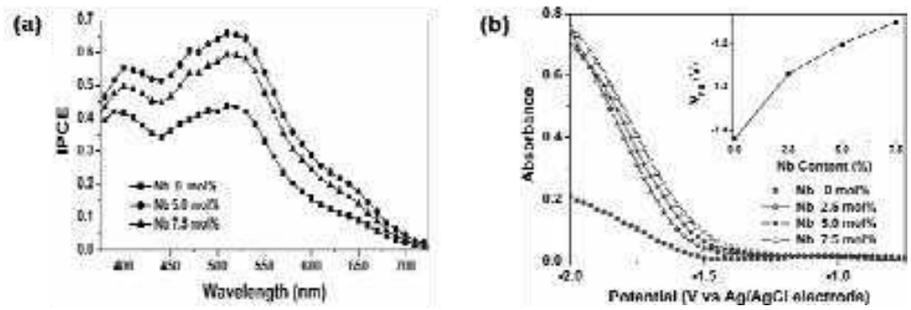

Fig. 13. (a) Action spectra of the dye-sensitized solar cells based on the undoped and Nb-doped TiO_2 electrodes. (b) Optical absorbance at 870 nm of undoped and Nb-doped TiO_2 films measured as a function of applied potential. Inset shows the flat-band potential of the samples as a function of the Nb contents

The reasons leading to a higher photocurrent for the solar cells based on Nb-doped TiO_2 are revealed according to the measurements on photocurrent action spectra and flat-band potential (V_{fb}). The action spectra are shown in Fig. 13, which present a significant enhancement in the IPCE of the DSCs based on the Nb-doped TiO_2 electrodes compared with that of the undoped one. The improvement can be attributed to the enhanced electron injection and charge transfer efficiency as well as the slightly higher amount of dye absorption as listed in Table 4. It has been reported that when the dye uptake increased 1.2 times, the IPCE only increased approximately 3% (Redmond & Fitzmaurice, 1993). Thus, the intrinsic increase in the photocurrent and IPCE are primarily due to the enhanced electron injection and transfer ability of the Nb-doped TiO_2. The effects caused by the Nb doping on electron injection, transfer and recombination of the DSCs would be discussed via the studies of flat-band potential and electrochemical impedance spectra as follows.

Photocurrent generation depends on electron injection, charge transfer, and charge recombination processes. Here the effect of the Nb doping on the above factors is qualitatively

discussed. The different positions of the excited energy level of the dye and the conduction band minimum (CBM) of the semiconductor are essential to the electron injection. Central to an understanding of the band energetics of a semiconductor electrode is the determination of flat-band potential (V_{fb}). As shown in Fig. 13b, the results indicate a positive shift of the flat-band potential with the increasing of Nb content. Consequently, the driving force for electron injection, E_{fb} – LUMO (the lowest unoccupied molecular orbital energy level) (Kron et al., 2003), is increased by the Nb doping, which correspondingly makes contribution to the enhancement of electron injection efficiency. Meanwhile, the open current potential (V_{oc}) of DSCs is dependent on the difference of the flat-band potential of TiO_2 and the redox potential of I^-/I_3^- couple. Therefore, the V_{oc} of the DSCs would decrease due to the positive shift of V_{fb}, as shown in Fig. 12 and Table 4. By optimally selecting the photoanode material, dye and electrolyte, the photocurrent density can be improved without significantly lowering the V_{oc}. One approach to increase V_{oc} is to adjust the redox potential to a more positive value (Han et al., 2004), while the dye's ground state potential should be positive enough comparing with the redox potential to make sure the efficient dye regeneration rate. Another approach is to choose a more efficient sensitizer, and then more electrons are injected to the photoanode, raising the Fermi level of the oxide and thus shift its potential.

The J_{sc} improvement is also related to the charge transfer ability. After the Nb doping, the charge compensation of Nb^{5+} in substitution to Ti^{4+} is achieved either by the creation of one Ti cation vacancy per four Nb introduced or by the stoichiometric reduction of Ti^{4+} to Ti^{3+} per Nb introduced.

$$\frac{1}{2}Nb_2O_5 + Ti_{Ti}^{x} \rightarrow Nb_{Ti}^{\bullet} + \frac{1}{4}V_{Ti}^{'''} + TiO_2 + \frac{1}{4}O_2 \quad (1)$$

$$\frac{1}{2}Nb_2O_5 + Ti_{Ti}^{x} \rightarrow Nb_{Ti}^{\bullet} + Ti_{Ti}^{'} + \frac{5}{4}O_2 \quad (2)$$

The occurrence of one or the other of two scenarios depends on the synthetic conditions and Nb concentration. High oxidative synthetic condition and low Nb content might play in favor of the scenario corresponding to Equation 1 because cations would be maintained in their higher oxidation state, whereas scenario corresponding to Equation 2 should be considered in low oxidative synthesis condition and high Nb concentrations. Here, the reactions occurred in a sealed autoclave with a rather low oxidative circumstance and the Nb contents are quite high (>2.5 mol%), thus the occurrence here is in favor of the scenario corresponding to Equation 2 and this has been demonstrated by Hirano and Matsushima (Nakamura et al., 2003). Consequently, one excess electron in the Ti 3d orbital due to each Nb^{5+} substituting for Ti^{4+} raises the electron concentration.

The enhancement of electron transfer ability was discussed on the basis of theoretical model of the electrical conductivity, which is based on the equation of $\sigma = ne\mu$, where e is elementary charge, n denotes the concentration of electrons, and μ is the electron mobility. The increasing of the electron concentration enhances the electron conductivity, and the improved electron transport efficiency results in the increase of the photocurrent density. However, the electron mobility decreased rapidly at high defect concentration due to the electron scattering by the defects. The severe defects increase charge recombination and that would become the dominant factor when the Nb content reaches a high level. The mechanism for electron transport through mesoporous TiO_2 is still a hotly debated topic. Deducing the exact

mechanism through experimental and theoretical investigations is complicated, partly because of the apparent inability to systematically vary individual parameters without influencing others. Fortunately, there have been much experimental and theoretical evidence that supports the notion that the electron transport is governed by a trapping-detrapping process of electrons from the sub-bandgap states (Longo et al., 2002). In the DSC system, one dye molecule transfers one electron to Ti^{4+} $3d^0$ of TiO_2, and then one Ti^{3+} $3d^1$ is generated. The energy gap between the Ti^{4+} $3d^0$ band and the Ti^{3+} $3d^1$ energy level is rather shallow, and the electron at Ti^{3+} $3d^1$ is easy to be transferred to the neighboring Ti^{4+} instead of being trapped to form space charge. This wonderful feature makes the loose-packed anatase TiO_2 be an excellent dye-sensitized electrode material. By doping Nb into the TiO_2 in this work, the Ti^{3+} $3d^1$ states existing in the nanocrystals increase the electron concentration, and these Ti^{3+} $3d^1$ states plus Nb^{5+} $4d^0$ make the band structure near conduction band minimum (CBM) more dispersed to enhance the mobility of the excited electrons. However, Ti^{3+} can also be the electron traps, when the TiO_2 has a very poor crystallinity or excessive imperfects. Furthermore, the results shown in Fig. 14 indicate that the resistance of powder drops sharply at the beginning of doping and changes slightly when the Nb content exceeds 5.0 mol%. This result certifies the reason of J_{sc} improvement discussed above.

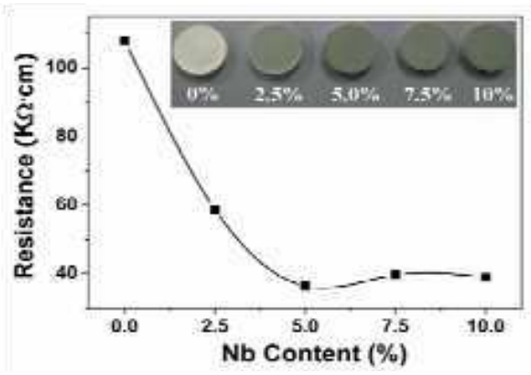

Fig. 14. Powder resistance of the as-prepared undoped and Nb-doped TiO_2. Inset shows the color change after Nb-doping

The internal resistances of DSCs were studied via electrochemical impedance spectroscopy (EIS) in the frequency range of 0.1 Hz – 100 kHz, and with alternating current amplitude of 10 mV. Fig. 15 shows the EIS results at forward bias of the open-circuit voltage under light irradiation and the results were represented as Nyquist plots. The responses in the frequency regions around 10^4, 10^3, 10 and 0.1 – 1 Hz are assigned to charge transfer processes occurring at the Pt/electrolyte interface, TiO_2 /TiO_2 particles interface, TiO_2/dye/electrolyte interface and the Nernst diffusion within the electrolyte, respectively. The relative low resistance between Pt/electrolyte interface results in an unobvious semicircle at the frequency ω_1 = 14.7 kHz. The border between the arcs of ω_2 and ω_3 was vague for the undoped TiO_2 electrode with the severe overlap between ω_2 and ω_3 resulting from the relative high resistance between TiO_2 particles. In contrast, the borders of the Nb-doped samples are clear. Obviously, the second semicircle at the frequency ω_2 = 1.2 kHz become smaller with increasing of Nb content (see Fig. 9b), owing to the enhanced electron conductivity. The third semicircle at the frequency ω_3 = 4.5 Hz expanded with the Nb content increasing from 2.5 mol% to 7.5 mol%. The raise of resistance at the TiO_2/dye/electrolyte interface is beneficial for suppressing the charge recombination at the interface, which can compensate the drop of V_{oc} caused by the positive

shift of flat-band potential. In Fig. 12, the V_{oc} of the cell based on the 7.5 mol% Nb-doped TiO_2 is close to than of the 5.0 mol% one, due to the greater compensation. However, the result at the Nb content of 10.0 mol% is abnormal which may because the severe defects became the recombination centers and hindered the charge transfer. The EIS results mentioned above confirm the mechanism of improvement.

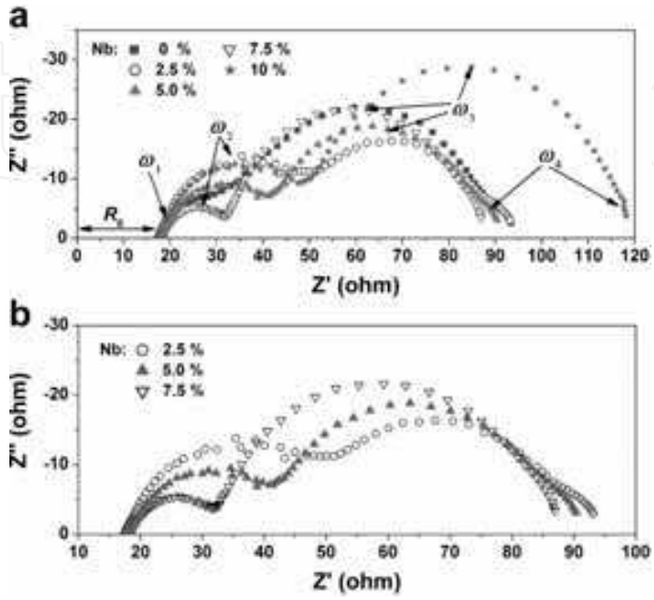

Fig. 15. Electrochemical impedance spectra of dye-sensitized solar cells based on the undoped and Nb-doped TiO_2 electrodes

In this section, the Nb-doped TiO_2 nanocrystalline powders were demonstrated to be an *electron-injection and transport favored semiconductor* to enhance the performance of dye-sensitized solar cells. The improvement was ascribed to the enhanced electron injection and transfer efficiency caused by positive shift of flat-band potential (V_{fb}) and increased powder conductivity, and the mechanism was verified by powder resistance and EIS analyses. Such systematic investigation on the effect of the Nb doping will provide valuable insight on designing the high-performing DSCs.

3.4 Synthesis and application of TiO_2 | ZnO: Ti | ZnO in photocatalysis and DSCs

TiO_2 hollow spheres with a hybrid composition were prepared by a hydrated-salt assisted solvothermal (HAS) strategy. In this method, a metallorganic Ti source reacts with the water that is slowly released from a hydrated salt of another metal, and hybrid metal oxides are obtained forming the desired nano-heterojunction structure of *semiconductor* | *semimetal* | *semiconductor* (*e.g.* TiO_2|ZnO:Ti|ZnO). We also report the photocatalytic activity and photovoltaic efficiency of a DSC fabricated with TiO_2/ZnO spheres demonstrating improved performance.

The hollow spherical morphology of the sample has been revealed by transmission electron microscopy (TEM). Also evident from Fig. 16b is the nanocrystallites in the shell of spheres, and the selected area electron diffraction (SAED) image (Fig. 16c) indicates the nanocrystallites are random in orientation. Energy-dispersive X-ray spectroscopy (EDS) shown in Fig. 16d determines the Zn content in the product to be 1.1 atomic%. According to

EXAFS spectroscopy, Zn^{2+} segregation occurs when the Zn concentration is above 0.1 atomic% in nanocrystalline anatase TiO_2 (Bouchet et al., 2003), which is reasonable in view of the large mismatch in the charge and the ionic radius between Ti^{4+} (0.61 Å) and Zn^{2+} (0.74 Å). Therefore, Zn^{2+} apparently has difficulty in entering the TiO_2 lattice and is likely to form very small crystallites that are incorporated into the TiO_2/ZnO composite in the hollow spheres. Such ZnO nanocrystals located between TiO_2 nanocrystals are expected to have a beneficial effect on electron mobility and charge separation.

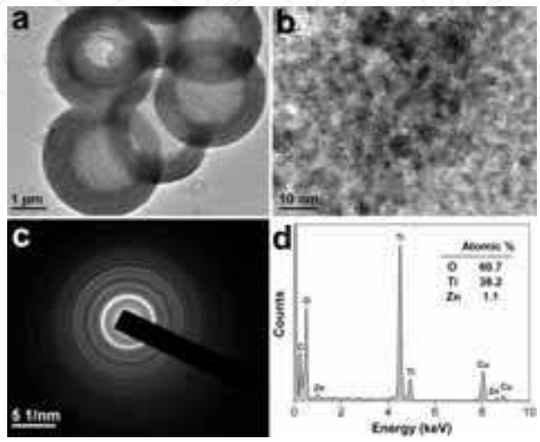

Fig. 16. (a, b) TEM images, (c) selected area electron diffraction (SAED) image, and (d) energy-dispersive X-ray spectroscopy (EDS) of the TiO_2/ZnO spheres

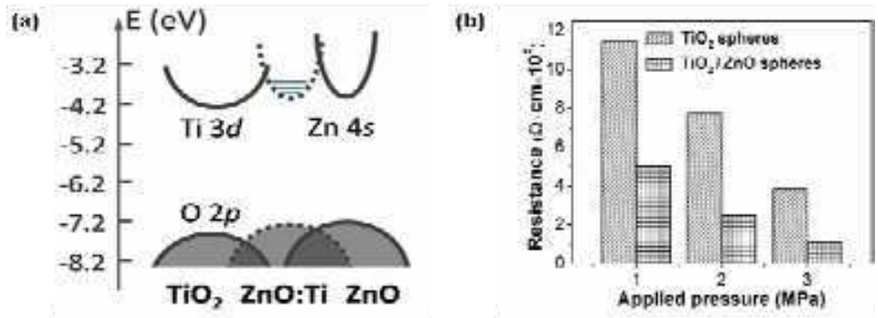

Fig. 17. (a) Schematic band structure of TiO_2|ZnO:Ti|ZnO heterojunction, (b) Powder resistances of the TiO_2/ZnO spheres and TiO_2 hollow spheres

As mentioned above, ZnO and TiO_2 have similar band structures, and charge can be easily transferred at their interface. As is well known, the smaller effective mass (m^*) of electrons implies the higher electron mobility (μ). Since the conduction band of TiO_2 originates from the *d*-orbital, which has a narrow bandwidth and a large m^* (~10 m_e), whereas the conduction band of ZnO has an *s*-orbital character giving rise to a much smaller m^* (~0.2 m_e) (Roh et al., 2006). Therefore, ZnO has a much higher electron mobility than TiO_2, which should have a beneficial effect on electron transport in the hybrid TiO_2/ZnO spheres. Moreover, although Zn^{2+} has a very small solubility in TiO_2, Ti^{4+} can dissolve up to 4 mol% in ZnO (Lin et al., 2005). Therefore, in the hybrid spheres, there is likely to exist a TiO_2/ZnO interface, Ti-doped ZnO (ZnO:Ti), which is a well-known TCO. Overall, the hybrid composite could achieve the schematic band structure configuration shown in Fig. 17a. Such

a construct of $TiO_2|ZnO:Ti|ZnO$ is suitable for charge separation and electron transport, so enhanced performance in both photocatalysis and DSCs can be expected. To demonstrate the beneficial effect of ZnO addition on electron transport, we compared the resistance of powder compacts of TiO_2/ZnO spheres and TiO_2 hollow spheres with comparable radius and shell thickness (These spheres have a comparable morphology and surface area as the hybrid TiO_2/ZnO spheres.). These compacts were cold-pressed under various pressures. As shown in Fig. 17b, regardless of compaction pressures, the TiO_2/ZnO hybrid compacts are always less resistive than nonhybrid TiO_2 compacts.

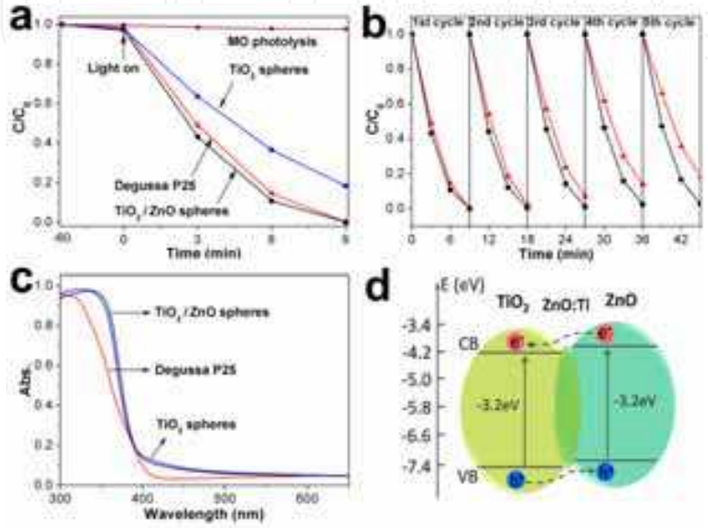

Fig. 18. (a) photocatalytic degradation of MO (10 mg L^{-1}) over TiO_2/ZnO spheres (●), TiO_2 hollow spheres (■), Degussa P25 (▲) and without catalyst (★), (b) cycling experiments of MO degradation over TiO_2/ZnO spheres (●) and Degussa P25 (▲), (c) UV-vis diffuse reflectance spectra of the TiO_2/ZnO spheres, TiO_2 hollow spheres and Degussa P25, and (d) schematic illustration of the band structure and charge separation in TiO_2/ZnO hybrid

To demonstrate the beneficial effect of ZnO addition on photocatalysis, the photocatalytic activity of the hybrid TiO_2/ZnO spheres is compared with similar TiO_2 hollow spheres using the methyl orange (MO) assay. Degussa P25, a highly effective photocatalyst often considered as the gold standard in this field, is also used as the reference. As shown in Fig. 18a, after UV irradiation for 9 min, MO was totally bleached over the TiO_2/ZnO spheres, whereas only 80% of MO was degraded over TiO_2 hollow spheres. The hybrid spheres also compared favorably with P25, and are more robust than P25 for repeated reuse (Fig. 18b). The superior performance of the hybrid spheres compared to P25 is probably attributed to a higher specific surface area (150 $m^2 g^{-1}$ vs. 50 $m^2 g^{-1}$) and more efficient light harvesting by the hollow spheres. On the other hand, since TiO_2 spheres and hybrid TiO_2/ZnO spheres have very similar UV-vis absorption and surface area, their different photocatalytic activities must be attributed to the differences in charge separation and electron transport caused by ZnO. According to the schematic band diagram of the $TiO_2|ZnO:Ti|ZnO$ heterojunction (Fig. 18d), electrons created in the conduction bands (CB) of TiO_2 and ZnO and holes in the valence bands (VB) can be separated at the heterojunctions due to the favorable energy bias between the two sides (Zhang et al., 2009). This reduces electron-hole recombination and maintains the requisite electron/hole populations required for photocatalytic reactions with organic dyes . In

addition, the lower resistance caused by ZnO addition (Fig. 17b) indicates that electron/hole transport is facilitated which should also favor photocatalytic activity. Incidentally, the similar absorption spectra of TiO_2 hollow spheres and TiO_2/ZnO spheres provide further evidence that few Zn^{2+} ions enter the TiO_2 lattice. Otherwise, aliovalent substitution would have created substitutional and charge-compensating point defects that affect optical absorption.

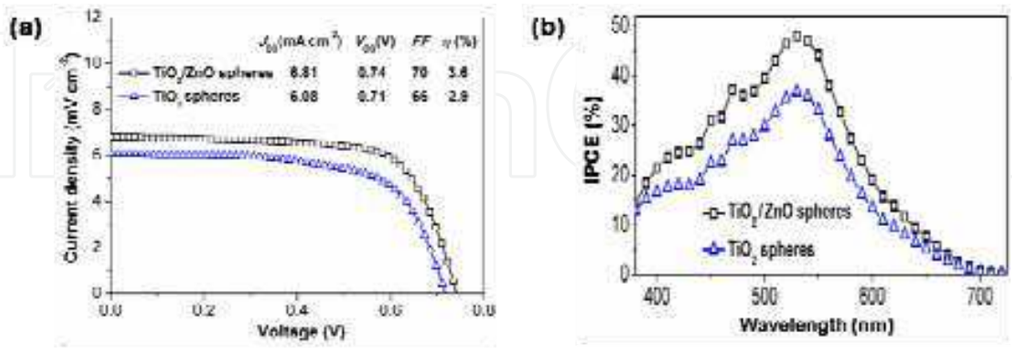

Fig. 19. (a) Photocurrent density-voltage curves, (b) action spectra of the DSCs with anodes made of TiO_2/ZnO spheres and TiO_2 hollow spheres

When used as the anode material to fabricate DSCs, enhanced performance can also been achieved. The photocurrent density-voltage (*J-V*) curves are shown in Fig. 19a. The energy-conversion efficiency increased from 2.9 % for TiO_2 hollow spheres to 3.6 % for hybrid TiO_2/ZnO spheres. This is primarily due to the increased photocurrent density, as well as the higher photovoltage and fill factor, which is not always easy to achieve by impurity doping only. In this case, the inhibition of electron back transfer from TiO_2 to the redox electrolyte (I_3^-) by the heterojunctions may contribute to the improvement in the photovoltage and fill factor (Kay & Gratzel, 2002). As shown in Fig. 19b, the incident-photon-to-current efficiency (IPCE) of the cell with a hybrid electrode is higher than that with a TiO_2 (hollow spheres) electrode at all wavelengths. Since there is only a slight difference in the dye adsorption between these two electrodes, and the influence of dye adsorption is known to be relatively minor (Ma et al., 2005), the main reason for the increase in the photocurrent density and IPCE in the cells with hybrid electrodes may be attributed to their enhanced electron transport efficiency. Under the solar illumination, the injected electrons in the Ti^{4+} 3*d* states transfer easily to the Zn^{2+} 4*s* states in the composite structure of TiO_2|ZnO:Ti|ZnO. Such a band-structure-matched heterojunction can be imaged as the "bridge" for electrons to transport from here to there. The enhanced electron transport efficiency raises the photocurrent density, results in the improvement of energy-conversion efficiency.

In conclusion, a new composite construct of *TiO_2 | semimetal | semiconductor* with a hollow spherical geometry with a hybrid TiO_2/ZnO composition is proposed for solar energy utilization. The hybrid TiO_2/ZnO spheres exhibit a higher photocatalytic activity and enhanced energy-conversion efficiency for the DSC. These improvements are ascribed to the enhanced charge-separation and electron-transport efficiencies made possible by the nano-heterojunction structure of TiO_2|ZnO:Ti|ZnO.

4. Summary

Over the past decades, the tremendous effort put into TiO_2 nanomaterials has resulted in a rich database for their synthesis, properties, modifications, and solar applications. The synthesis

and modifications of TiO_2 nanomaterials have brought new properties and new applications with improved performance via solar energy utilization techniques in our lab. Meanwhile, TiO_2 nanomaterials also exhibit size-dependent as well as shape- and structure-dependent optical, electronic, thermal, and structural properties, as reported by other groups. TiO_2 nanomaterials have continued to be highly active in photocatalytic and photovoltaic applications, and they also demonstrate new applications including electrochromics, sensing, and hydrogen storage. This steady progress has demonstrated that TiO_2 nanomaterials are playing and will continue to play an important role in the protections of the environment and in the search for renewable and clean energy technologies.

5. References

Bouchet, R. ; Weibel, A. & Knauth, P. (2003). EXAFS study of dopant segregation (Zn, Nb) in nanocrystalline anatase (TiO_2). *Chem. Mater.,* 15, 26, 4996-5002, 0897-4756

Chen, X.; Mao, S. S. (2007). Titanium dioxide nanomaterials: Synthesis, properties, modifications, and applications. *Chem. Rev.* 107, 7, 2891–2959, 0009-2665

Chung, L.; Chen, J. C. & Tseng, C. J. (2008). Preparation of TiO_2-doped ZnO films by radio frequency magnetron sputtering in ambient hydrogen-argon gas, *Appl. Surf. Sci.*, 255, 5, 2494-2499, 0169-4332

Furubayashi, Y.; Hitosugi, T. & Yamamoto, Y. (2005). A transparent metal: Nb-doped anatase TiO_2. *Appl. Phys. Lett.*, 86, 25, 252101, 0003-6951

Ghosh, G.; Patra, A. (2007). Influence of surface coating on physical properties of TiO_2/Eu^{3+} nanocrystals. *J. Phys. Chem. C,* 111, 19, 7004-7010, 1932-7447

Han, L.; Koide, N. & Chiba, Y. (2004). Modeling of an equivalent circuit for dye-sensitized solar cells. *Appl. Phys. Lett.*, 84, 13, 2433-2435, 0003-6951

Hua, Z. L.; Wang, X. M. & Shi, J. L. (2006). Solvent effect on microstructure of yttria-stabilized zirconia (YSZ) particles in solvothermal synthesis. *J. Eur Ceram. Soc.*, 26, 12, 2257–2264, 0955-2219

Ikeda, M.; Li, J. G. & Kobayashi, N. (2008). Phase formation and luminescence properties in Eu^{3+}-doped TiO_2 nanoparticles prepared by thermal plasma pyrolysis of aqueous solutions. *Thin Solid Films,* 516, 19, 6640–6644, 0040-6090

Kay, A.; Gratzel, M. (2002). Dye-sensitized core-shell nanocrystals: Improved efficiency of mesoporous tin oxide electrodes coated with a thin layer of an insulating oxide. *Chem. Mater.,* 14, 7, 2930-2935, 0897-4756

Kron, G.; Rau, U. & Werner, J. H. (2003). Influence of the Built-in Voltage on the Fill Factor of Dye-Sensitized Solar Cells. *J. Phys. Chem. B*, 107, 48, 13258-13261, 1520-6106

Li, J.; Zeng, H. C. (2007). Hollowing Sn-doped TiO_2 nanospheres via Ostwald ripening, *J. Am. Chem. Soc.*, 129, 51, 15839–15847, 0002-7863

Lin, J.; Yu, J. C. (1998). An investigation on photocatalytic activities of mixed TiO_2-rare earth oxides for the oxidation of acetone in air. *J. Photochem. & Photobio. A: Chem.,* 116, 1, 63-67, 1010-6030

Lin, S. S.; Huang, J. L. & Sajgalik, P. (2005). The properties of Ti-doped ZnO films deposited by simultaneous RF and DC magnetron sputtering. *Surface and Coatings Technology*, 191, 3, 286-292, 0257-8972

Lin, X. P.; Wu, J. J. & Huang, F. Q. (2009). Novel antimonate photocatalysts MSb_2O_6 (M= Ca, Sr and Ba): a correlation between packing factor and photocatalytic activity. *Phys.Chem.Chem.Phys.,* 11, 43, 10047–10052, 1463-9076

Longo, C.; Nogueira, A. F. & Cachet, H. (2002). Solid-state and flexible dye-sensitized TiO_2 solar cells: a study by electrochemical impedance spectroscopy. *J. Phys. Chem. B,* 106, 23, 5925-5930, 1520-6106

Lü, X. J.; Mou, X. L. & Huang, F. Q. (2010). Improved-performance dye-sensitized solar cells using Nb-doped TiO_2 electrodes: efficient electron injection and transfer. *Adv. Funct. Mater.,* 20, 3, 209-515, 1616-301X

Ma, T. L.; Akiyama, M. & Abe, E. (2005). High-efficiency dye-sensitized solar cell based on a nitrogen-doped nanostructured titania electrode. *Nano. Lett.,* 5, 12, 2543-2547, 1530-6984

Moon, Y. T.; Park, H. K. & Seog, I. S. (1995). Preparation of monodisperse and spherical zirconia powders by heating of alcohol-aqueous salt-solutions. *J. Am. Ceram. Soc.* 1995, 78, 10, 2690–2694, 0002-7820

Nakamura, R.; Imanishi, A. & Murakoshi, K. (2003). In situ FTIR studies of primary intermediates of photocatalytic reactions on nanocrystalline TiO_2 films in contact with aqueous solutions. *J. Am. Chem. Soc.,* 125, 24, 7443-7450, 0002-7863

Redmond, G.; Fitzmaurice, D. (1993). Spectroscopic determination of flat band potentials for polycrystalline TiO_2 electrodes in nonaqueous solvents. *J. Phys. Chem.,* 97, 7, 1426-1430, 0022-3654

Roh, S.; Mane, R. & Han, S. (2006). Achievement of 4.51% conversion efficiency using ZnO recombination barrier layer in TiO_2 based dye-sensitized solar cells. *Appl. Phys. Lett.,* 89, 25, 253512, 0003-6951

Sharma, R. K.; Bhatnagar, M. C. & Sharma, G. L. (1998). Mechanism in Nb doped titania oxygen gas sensor. *Sensors and Actuators B: Chem.*, 46, 3, 194-201, 0925-4005

Sirachaya, K. N. A.; Okorn M. & Piyasan P. (2006). Solvothermal synthesis of ZnO with various aspect ratios using organic solvents. *Cryst. Growth & Des.*, 6, 11, 2446–2450, 1528-7483

Stone, B. T.; Costa, V. C. & Bray, K. L. (1997). In situ dehydroxylation in Eu^{3+}-doped sol-gel silica. *Chem. Mater.,* 9, 11, 2592-2598, 0897-4756

Tian, G. H.; Fu, H. G. & Xin, B. F. (2008). Preparation and characterization of stable biphase TiO_2 photocatalyst with high crystallinity, large surface area, and enhanced photoactivity. *J. Phys. Chem. C*, 112, 8, 3083–3089, 1932-7447

Wu, J. J.; Lü, X. J. & Huang, F. Q. (2009). Dielectric constant-controlled solvothermal synthesis of photocatalyst TiO_2 with tunable crystallinity: A strategy for solvent-selection. *Eur. J. Inorg. Chem.*, 2009, 19, 2789–2795, 1434-1948

Wu, J. J.; Lü, X. J. & Huang, F. Q. (2010). Crystallinity control on photocatalysis and photoluminescence of TiO_2-based nanoparticles. *J. Alloy. Compd.,* 496, 1, 234-240, 0925-8388

You, H. P.; Nogami, M. (2004). Optical properties and local structure of Eu^{3+} ions in sol-gel TiO_2-SiO_2 glasses. *J. Phys. Chem. B,* 108, 32, 12003-12008, 1520-6106

Yu, J. G. & Wang, G. H. (2007). Effects of hydrothermal temperature and time on the photocatalytic activity and microstructures of bimodal mesoporous TiO_2 powders. *Appl. Catal. B: Environ*, 69, 3, 171–180, 0926-3373

Zhang, J.; Sun, L. D. & Yan, C. H. (2002). Control of ZnO morphology via a simple solution route, *Chem. Mater.*, 14, 10, 4172–4177, 0897-4756

Zhang, L. S.; Wong, K. H. & Wong, P. K. (2009). AgBr-Ag-Bi_2WO_6 nanojunction system: A novel and efficient photocatalyst with double visible-light active components. *Appl. Catal. A: Gen.,* 363, 2, 221-229, 0926-860X

Zhang, Q. F.; Dandeneau, C. S. & Zhou, X. Y. (2009). ZnO nanostructures for dye-sensitized solar cells. *Adv. Mater.*, 21, 41, 4087-4108, 0935-9648

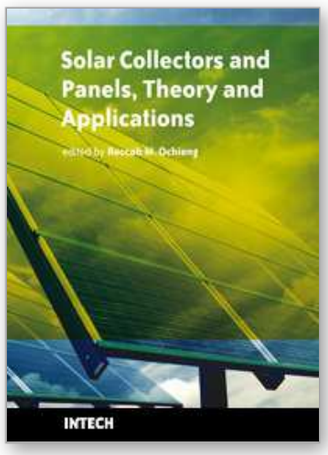

Solar Collectors and Panels, Theory and Applications
Edited by Dr. Reccab Manyala

ISBN 978-953-307-142-8
Hard cover, 444 pages
Publisher Sciyo
Published online 05, October, 2010
Published in print edition October, 2010

This book provides a quick read for experts, researchers as well as novices in the field of solar collectors and panels research, technology, applications, theory and trends in research. It covers the use of solar panels applications in detail, ranging from lighting to use in solar vehicles.

How to reference
In order to correctly reference this scholarly work, feel free to copy and paste the following:

Fuqiang Huang (2010). Titanium Dioxide Nanomaterials: Basics and Design, Synthesis and Applications in Solar Energy Utilization Techniques, Solar Collectors and Panels, Theory and Applications, Dr. Reccab Manyala (Ed.), ISBN: 978-953-307-142-8, InTech, Available from: http://www.intechopen.com/books/solar-collectors-and-panels--theory-and-applications/titanium-dioxide-nanomaterials-basics-and-design-synthesis-and-applications-in-solar-energy-utilizat

INTECH
open science | open minds

InTech Europe
University Campus STeP Ri
Slavka Krautzeka 83/A
51000 Rijeka, Croatia
Phone: +385 (51) 770 447
Fax: +385 (51) 686 166
www.intechopen.com

InTech China
Unit 405, Office Block, Hotel Equatorial Shanghai
No.65, Yan An Road (West), Shanghai, 200040, China
中国上海市延安西路65号上海国际贵都大饭店办公楼405单元
Phone: +86-21-62489820
Fax: +86-21-62489821

IntechOpen